

Effects of Reynolds number on leading-edge vortex formation dynamics and stability in revolving wings

Long Chen^{1,†}, Luyao Wang¹, Chao Zhou², Jianghao Wu² and Bo Cheng³

¹College of Sciences, Northeastern University, Shenyang, Liaoning 110819, PR China

²School of Transportation Science and Engineering, Beihang University, Beijing 100191, PR China

³Department of Mechanical Engineering, Pennsylvania State University, University Park, PA 16801, USA

(Received 25 April 2021; revised 21 September 2021; accepted 24 October 2021)

The mechanisms of leading-edge vortex (LEV) formation and its stable attachment to revolving wings depend highly on Reynolds number (Re). In this study, using numerical methods, we examined the Re dependence of LEV formation dynamics and stability on revolving wings with Re ranging from 10 to 5000. Our results show that the duration of the LEV formation period and its steady-state intensity both reduce significantly as Re decreases from 1000 to 10. Moreover, the primary mechanisms contributing to LEV stability can vary at different Re levels. At $Re < 200$, the LEV stability is mainly driven by viscous diffusion. At $200 < Re < 1000$, the LEV is maintained by two distinct vortex-tilting-based mechanisms, i.e. the planetary vorticity tilting and the radial–tangential vorticity balance. At $Re > 1000$, the radial–tangential vorticity balance becomes the primary contributor to LEV stability, in addition to secondary contributions from tip-ward vorticity convection, vortex compression and planetary vorticity tilting. It is further shown that the regions of tip-ward vorticity convection and tip-ward pressure gradient almost overlap at high Re . In addition, the contribution of planetary vorticity tilting in LEV stability is Re -independent. This work provides novel insights into the various mechanisms, in particular those of vortex tilting, in driving the LEV formation and stability on low- Re revolving wings.

Key words: swimming/flying, vortex dynamics

1. Introduction

The formation and stable attachment of a leading-edge vortex (LEV), which give rise to the absence of stall, are prominent features of insect flight (Ellington *et al.* 1996; Wu

† Email address for correspondence: chenlong@mail.neu.edu.cn

& Sun 2004) and unidirectional revolving wings at high angles of attack (α) (Sun & Wu 2004; Kim & Gharib 2010; Ozen & Rockwell 2012; Cheng *et al.* 2013; Garmann, Visbal & Orkwis 2013; Wolfinger & Rockwell 2014; Carr, DeVoria & Ringuette 2015; Chen, Wu & Cheng 2019). The attached LEV enables a sustained high lift generation, which is the underpinning of the hovering capacity and manoeuvrability of insect flight (Dickinson, Lehmann & Sane 1999; Sane 2003; Sun 2014). In contrast, the LEV generated by high- α translating wings quickly detaches once it reaches peak intensity and a normal stall occurs thereafter (Dickinson & Gotz 1993; Jardin & David 2014). There is no doubt that the revolving nature leads to the distinctly different LEV behaviours between revolving wings and their translating counterparts. In the literature, the stable attachment of LEV on revolving wings has been studied extensively, and several hypotheses have been proposed to explain the mechanisms that contribute to LEV stability.

One of the most well-known hypotheses for LEV stability is the spanwise vorticity convection, driven by the tip-ward spanwise flow. The vorticity generated from the leading edge can be transported towards the wing tip under this spanwise convection, therefore keeping the vorticity within the LEV from being further accumulated. Ellington *et al.* (1996) first proposed this hypothesis and postulated that the spanwise flow can be generated by a spanwise pressure gradient. However, this hypothesis was questioned subsequently by several research groups using either experiment (Birch & Dickinson 2001; Birch, Dickson & Dickinson 2004; Cheng *et al.* 2013) or simulation (Shyy & Liu 2007), in which no evidence of significant spanwise flow is observed at a Reynolds number (Re) around 100. Birch *et al.* (2004) and Shyy & Liu (2007) both showed that the spanwise flow, as well as the spanwise vorticity convection, occur only when Re reaches 1000. On the other hand, Lentink & Dickinson (2009) theorized and experimentally investigated the effects of rotational accelerations, i.e. centrifugal and Coriolis acceleration, on LEV stability, and postulated that the formation of the spanwise flow behind the LEV is due to the Ekman pumping phenomenon. They further proposed that rotational accelerations are inversely proportional to aspect ratio (AR) and thus a wing with smaller AR possesses stronger rotational accelerations and a more stable LEV. However, their work still did not affirm a specific mechanism for the LEV stability and does not apply when significant spanwise flow is absent, for example, at $Re = 100$.

Inspired by Lentink & Dickinson (2009), the role of Coriolis acceleration in LEV stability was further investigated by two research groups. Jardin & David (2015) and Jardin (2017) further supported that the Coriolis acceleration contributes to LEV stability, whereas Garmann *et al.* (2013) and Garmann & Visbal (2014) argued that the Coriolis acceleration is unlikely to stabilize the LEV, at least as a direct mechanism. It should be noted that the research of the two groups was conducted at different Re levels. Alternatively, Werner *et al.* (2019, 2020) mathematically related the tangential Coriolis acceleration with the radial tilting of planetary vorticity (PVT_r) and proposed that PVT_r can be a universal contributor to LEV stability in the ranges $Re = 110\text{--}1400$ and $AR = 3\text{--}7$. The PVT_r can be regarded as the reorientation of planetary vorticity into the spanwise direction, which produces vorticity opposite to that of the LEV.

For other hypotheses on LEV stability, Birch & Dickinson (2001) suggested that the tip-vortex-induced downwash can promote LEV stability since the LEV remains attached when fences are positioned along the leading edge to block the spanwise flow. The effective angle of attack of the wing can be reduced due to this downwash effect, preventing the LEV from shedding. Wojcik & Buchholz (2014) proposed a vorticity annihilation hypothesis to explain the unbalanced vorticity flux from the leading-edge shear layer, suggesting that the opposite-sign vorticity layer between the LEV and the wing surface regulates the unbalanced vorticity flux.

In general, the LEV on revolving wings is stabilized under complex vorticity dynamics, which may involve multiple interconnected mechanisms across different Re that still require a thorough examination. According to Jardin & Colonius (2018), the LEV dynamics also varies along the wing span, and depends on local radius (or Rossby number, Ro). Therefore, it is plausible that the relative contributions of the above-mentioned mechanisms can also vary along the spanwise direction. Moreover, the LEV stability (including the LEV bursting) is also dependent on Re (Lentink & Dickinson 2009). Notably, Harbig, Sheridan & Thompson (2013) defined a span-based Re_R to better predict the bursting of vortical structure in their study on the LEV stability of revolving wings with fruitfly geometry. They further applied this definition to decouple the effects of Re , AR and Ro on LEV stability and lift generation in revolving wings, but without focusing on the specific mechanisms of LEV stability (Bhat *et al.* 2019a,b). It is also noteworthy that previous studies on LEV dynamics mainly focus on its steady state when it already becomes approximately stable (i.e. without major shedding). Our previous studies, however, also emphasized the importance of the LEV formation process and the transient vorticity dynamics in understanding the LEV stability and the aerodynamics of real insect flights and flapping-wing micro air vehicles (FWMAVs) (Chen *et al.* 2019; Chen, Wu & Cheng 2020). However, the Re dependence of the LEV formation dynamics on revolving wings has not yet been studied.

In this work, as a follow-up of our previous studies (Chen *et al.* 2019, 2020), the transient vorticity dynamics on revolving wings at various Re were studied to fully elucidate the effects of Re on LEV formation dynamics and stability. The flow data were computed using the computational fluid dynamics (CFD) method with a fixed wing geometry. The wing started its rotation from stationary with a constant angular acceleration within a prescribed distance, followed by a constant-speed rotation. The wing geometry, kinematics and numerical methods are introduced in § 2. The effects of Re on vorticity dynamics are presented in § 3, starting with the LEV structure and intensity (§ 3.1). The vorticity transport mechanisms, including convection, vortex tilting and stretching, and diffusion, are further discussed in § 3.2, and a summary of Re effects on LEV stability is presented in § 3.3. Finally, our conclusions are presented in § 4.

2. Materials and methods

2.1. Wing geometry and kinematics

Following our previous simulations (Chen *et al.* 2020), the revolving wing was modelled by a rectangular rigid plate with an AR of 3, which is close to the average AR of most insects (Lentink & Dickinson 2009). The AR was defined as the ratio of span (b) over chord (c), and a root cutoff (r_0) of $0.9c$ was introduced, as shown in figure 1(a). The thickness of the wing was $0.03c$ and the angle of attack (α) was 45° throughout the rotation. A chord-normalized wing travelling distance (λ) at the radius of gyration (R_g) was employed to describe the revolving motion and LEV evolution, which are defined by

$$R_g = \sqrt{\int_0^{b+r_0} r^2 c \, dr / bc}, \quad (2.1)$$

$$\lambda = R_g \phi / c, \quad (2.2)$$

where ϕ is the revolving angle. The wing underwent a quick acceleration within a prescribed chord-normalized travelling distance (λ_a) of 0.5 and then maintained the

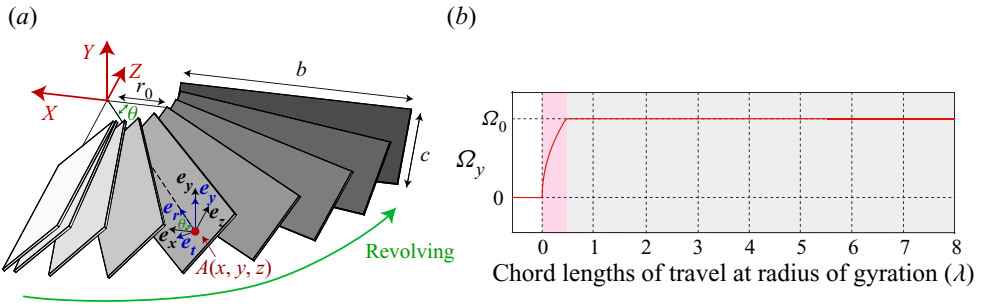


Figure 1. Schematics of wing geometry and kinematics: (a) the rectangular rigid wing model and (b) the revolving speed. The global and rotating Cartesian frames at a selected point $A(x, y, z)$ are shown by base axes (e_x, e_y, e_z) and (e_t, e_y, e_r) , respectively. The tangential (e_t) and radial (e_r) axes vary with the azimuth angle (θ) of point A .

Species	Span (mm)	f (Hz)	ϕ (deg.)	$\phi R_g/c$	Re_{est}
Wasp (<i>Encarsia formosa</i>)	0.7	370	120	4.4	18
Vegetable leafminer (<i>Liriomyza sativae</i>)	1.4	265	182	6.2	40
Fruitfly (<i>Drosophila</i>)	3	240	150	3.5	150
Hoverfly (<i>Episyrphus balteatus</i>)	7	175	85	2.3	250
Blue blowfly (<i>Calliphora erythrocephala</i>)	9.7	159	120	3.2	1000
Dronefly (<i>Eristalis tenax</i>)	12.7	182	120	3.2	2000
Bumblebee (<i>Bombus terrestris</i>)	17.3	156	150	2.8	4500
Hawkmoth (<i>Manduca sexta</i>)	54	27.3	120	2.6	6700

Table 1. Wing span, kinematics and estimated Reynolds number of typical insect species during hover. The span is measured on a single wing and ϕ denotes the full stroke angle.

constant revolving speed (Ω_0) until $\lambda = 8$ (figure 1b). Note that the total revolving angle was about 180° and no stable downwash induced by multiple rotations was involved here.

In this study, the reference velocity was the constant revolving velocity at R_g , and τ denoted the dimensionless time. The chord was selected as the length reference and thus Re was calculated as

$$Re = \Omega_0 R_g c / \nu, \tag{2.3}$$

where ν denoted the kinematic viscosity. According to the morphology and kinematics of insect wings (Weis-Fogh 1973; Mou, Liu & Sun 2011; Cheng & Sun 2016) (table 1), the Re of our research was limited to between 10 and 5000, corresponding to the estimated Reynolds numbers (Re_{est}) of most insect species during hover.

2.2. Numerical method and simulation set-up

The unsteady flow generated by low- Re revolving wings is governed by the three-dimensional (3-D) incompressible unsteady Navier–Stokes equations,

$$\left. \begin{aligned} \nabla \cdot \mathbf{u} &= 0, \\ \partial \mathbf{u} / \partial \tau + (\mathbf{u} \cdot \nabla) \mathbf{u} + \nabla p - \nabla^2 \mathbf{u} / Re &= 0, \end{aligned} \right\} \tag{2.4}$$

where \mathbf{u} and p denote the velocity and static pressure. The governing equation was discretized using a node collocated arrangement of primitive variables and then solved

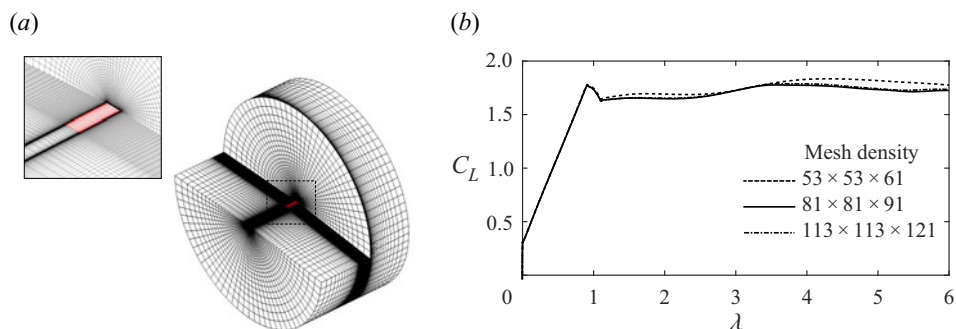


Figure 2. (a) The O–H computational mesh and (b) the validation of mesh density.

using an in-house solver. Based on the artificial compressibility method, the in-house solver implemented an implicit scheme with second-order spatial and time accuracy. Owing to the low- Re regime in our study, the flow was dominated by laminar structures, and therefore no turbulence model was included. For more information of the solver, please refer to Chen *et al.* (2020). An O–H (topology style) mesh was used in our numerical set-up to discretize the flow domain around the wing (figure 2a) and a thorough validation of the mesh was conducted based on a typical revolving motion at $Re = 1500$ and $\alpha = 45^\circ$. The mesh with a moderate density was employed, i.e. $81 \times 81 \times 91$ nodes in wing-normal, chordwise and spanwise directions (figure 2b). The domain size, first grid distance from wing surface and dimensionless time step were $30c$ (wing-normal and spanwise directions), $0.001c$ and 0.0075 , respectively. In addition, the accuracy of our numerical method was also proved in our previous studies on revolving wings (Chen *et al.* 2020) and pitching–flapping perturbed revolving wings (Chen *et al.* 2018; Wu *et al.* 2019), where a comparison of unsteady aerodynamic forces with dynamically scaled robotic wing experiments was conducted.

2.3. Data analysis

Owing to the rotational nature of the wing, the analysis of flow data and transient vorticity dynamics was carried out based on a set of rotating Cartesian frames (Cheng *et al.* 2013; Werner *et al.* 2019), as shown by the base axes (e_t , e_y , e_r) in figure 1(a). The local rotating Cartesian frame is defined according to the azimuth angle (θ) of the grid point and is fixed throughout the entire wing motion. As shown in figure 1(a), the tangential and radial axes of the local rotating Cartesian frame are perpendicular and parallel to the segment between the grid point and the centre of rotation and therefore rotate with the point of interest about the fixed vertical axis. Note that the positive tangential and radial directions are defined as the backward direction (with respect to the revolving motion) and the centripetal direction (with respect to the origin), respectively. All vector quantities in the global frame are therefore projected into the rotating Cartesian frames using the rotation matrix $\mathbf{J}(\theta)$,

$$\mathbf{J}(\theta) = \begin{bmatrix} \sin(\theta) & 0 & -\cos(\theta) \\ 0 & 1 & 0 \\ \cos(\theta) & 0 & \sin(\theta) \end{bmatrix}. \quad (2.5)$$

Given our definition of reference length and velocity (§ 2.1), the analysis of flow data and vorticity transport was conducted according to the non-dimensional Navier–Stokes

equation (2.6) and the non-dimensional vorticity transport equation (2.7) in the co-rotating frame:

$$d\mathbf{u}^*/d\tau = -\nabla p - \boldsymbol{\Omega} \times (\boldsymbol{\Omega} \times \mathbf{r}) - 2\boldsymbol{\Omega} \times \mathbf{u}^* + \nabla^2 \mathbf{u}^*/Re, \tag{2.6}$$

$$\partial \boldsymbol{\omega}^*/\partial \tau = -(\mathbf{u}^* \cdot \nabla) \boldsymbol{\omega}^* + (\boldsymbol{\omega}^* \cdot \nabla) \mathbf{u}^* + (2\boldsymbol{\Omega} \cdot \nabla) \mathbf{u}^* + \nabla^2 \boldsymbol{\omega}^*/Re. \tag{2.7}$$

Here $\mathbf{u}^* = \mathbf{u} - \boldsymbol{\Omega} \mathbf{r}$ and $\boldsymbol{\omega}^* = \boldsymbol{\omega} - 2\boldsymbol{\Omega}$ represent the relative velocity and vorticity in the co-rotating frame, and $\boldsymbol{\Omega}$ denotes the angular velocity of the wing. The first three terms on the right-hand side of (2.6) are pressure gradient, centrifugal acceleration and Coriolis acceleration that manipulate the motion of a fluid particle. In (2.7), the terms $-(\mathbf{u}^* \cdot \nabla) \boldsymbol{\omega}^*$, $(\boldsymbol{\omega}^* \cdot \nabla) \mathbf{u}^*$, $(2\boldsymbol{\Omega} \cdot \nabla) \mathbf{u}^*$ and $\nabla^2 \boldsymbol{\omega}^*/Re$ represent the convection, vortex tilting and stretching, planetary vorticity tilting, and diffusion, that determine the vorticity transport at a fixed position. Since the LEV formation and stability are usually represented by the evolution of radial vorticity, the radial component of (2.6) and (2.7) are thus the focus of our following discussion, as given by (2.8) and (2.9):

$$du_r^*/d\tau = \underbrace{-\partial p/\partial r}_{F_{pre}} + \underbrace{\Omega_y^2 r}_{F_{cen}} + \underbrace{2\Omega_y u_t^*}_{F_{cor}} + \nabla^2 u_r^*/Re, \tag{2.8}$$

$$\partial \omega_r^*/\partial \tau = -(\mathbf{u}^* \cdot \nabla) \omega_r^* + (\boldsymbol{\omega}^* \cdot \nabla) u_r^* + \underbrace{(2\Omega_y \partial u_r^*/\partial y)}_{PVT_r} + \underbrace{\nabla^2 \omega_r^*/Re}_D. \tag{2.9}$$

The radial components of pressure gradient, centrifugal acceleration and Coriolis acceleration are abbreviated as F_{pre} , F_{cen} and F_{cor} in our research. The first two terms on the right-hand side of (2.9) can be further expanded as:

$$-(\mathbf{u}^* \cdot \nabla) \omega_r^* = \underbrace{-u_t^* \partial \omega_r^*/\partial t}_{C_t} - \underbrace{u_y^* \partial \omega_r^*/\partial y}_{C_y} - \underbrace{u_r^* \partial \omega_r^*/\partial r}_{C_r}, \tag{2.10}$$

$$(\boldsymbol{\omega}^* \cdot \nabla) u_r^* = \underbrace{\omega_t^* \partial u_r^*/\partial t}_{T_{t \rightarrow r}} + \underbrace{\omega_y^* \partial u_r^*/\partial y}_{T_{y \rightarrow r}} + \underbrace{\omega_r^* \partial u_r^*/\partial r}_{S_r}. \tag{2.11}$$

Here, C_t , C_y and C_r denote the convection of radial vorticity due to tangential, vertical and radial flows; and $T_{t \rightarrow r}$ and $T_{y \rightarrow r}$ represent the vortex tilting of tangential and vertical vorticity components into the radial direction, whereas S_r is the vortex stretching (or compression) of radial vorticity component. The radial tilting of planetary vorticity (PVT_r) and the viscous diffusion are explicitly defined in (2.9). Our following discussion on LEV formation dynamics and stability is based on an examination of the spatial-temporal evolution of these vorticity transport components. Note that the gradient tensors in the rotating Cartesian frames can be calculated from their counterparts in the global frame using the chain rule.

The vorticity transport components at a specific grid point can be calculated according to (2.9)–(2.11). However, their overall impact should be estimated using an integration within the LEV region. Following our previous procedure (Chen *et al.* 2019, 2020), a series of 40 cylindrical slices (evenly distributed from root to tip) are introduced to cut through the flow domain (figure 3a). The LEV region within a specific cylindrical slice is outlined by the intersection of $Q > 1$ and $\omega_r^* < 0$ (figure 3b), where Q is the second invariant of velocity gradient (Jeong & Hussain 1995). The threshold of Q criteria is chosen by a sensitivity study. (Details can be found in the supplementary material available at <https://doi.org/10.1017/jfm.2021.950>).

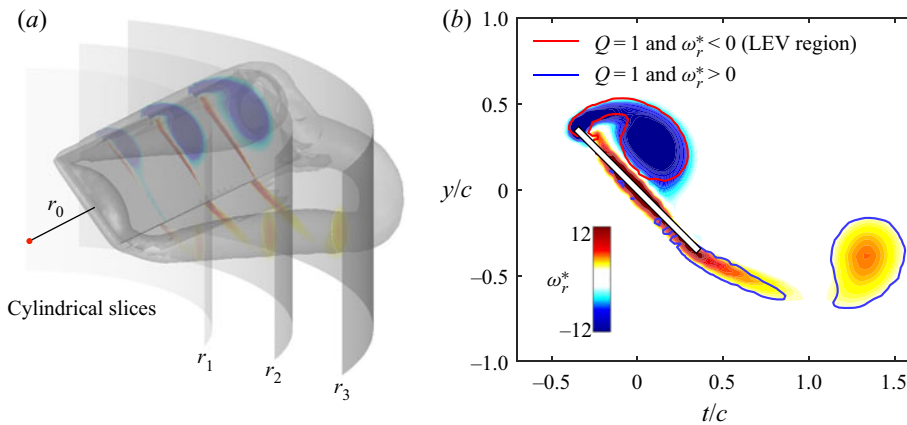


Figure 3. Schematics showing the definition of LEV region: (a) three representative cylindrical slices that discretize the vortical structure outlined by $Q = 1$ and (b) radial vorticity within the mid-span cylindrical slice. The Re and λ are 1500 and 1.5.

1017/jfm.2021.950.) Therefore, the LEV circulation on the i th t - y plane ($\Gamma(i)$) is estimated using the following equation:

$$\Gamma(j) = \sum_{\text{LEV}} \omega_r^*(t, y) dS(t, y). \tag{2.12}$$

Here, $dS(t,y)$ denotes the area element for the grid point at (t, y) in the cylindrical slice; and \sum_{LEV} infers that the summation is conducted within the LEV region defined above. The volumetric average of LEV intensity ($\tilde{\Gamma}$) is thus expressed as the average of $\Gamma(1)$ to $\Gamma(40)$.

3. Results

3.1. Leading-edge vortex intensity and structure

The Re effects on transient and stable LEV intensity are first examined (figure 4). Here, $\tilde{\Gamma}$ is used as a measure to characterize the LEV formation. Similar to our previous study at $Re = 1500$ (Chen *et al.* 2019), the LEV intensity of revolving wings with $Re > 500$ experiences a steep increase after the onset of the motion and then levels off while reaching the steady state. For revolving wings with $Re < 500$, an overshoot of LEV intensity is observed after the steep increase and thereafter $\tilde{\Gamma}$ falls back to the steady value. In general, $\tilde{\Gamma}$ becomes steady within the constant-speed revolving phase and the arrival timing of the stable LEV (in terms of the chord length of travel) increases with Re , e.g. $\lambda_c \approx 1.5$ ($Re = 10$), $\lambda_c \approx 3$ ($10 < Re < 200$) and $\lambda_c \approx 4$ ($200 < Re < 5000$). Here, λ_c represents the critical travel distance at R_g when arriving at the steady $\tilde{\Gamma}$. If not noted otherwise, we regard the arrival of steady $\tilde{\Gamma}$ as the achievement of a stable LEV in our following discussion. Note that, for revolving wings with $Re = 1000$ – 5000 , a slight increase of $\tilde{\Gamma}$ is observed at $\lambda > 4$, which was also seen in our previous research (Chen *et al.* 2019, 2020). However, this slight enhancement is less than 10 % of the stable LEV intensity, and thus is not considered when estimating λ_c . In addition to the transient $\tilde{\Gamma}$, the stable LEV intensity ($\tilde{\Gamma}_s$) also experiences an asymptotic trend over Re (figure 4b). A stronger stable LEV is generated on the revolving wing at a higher Re and an approximately linear trend over

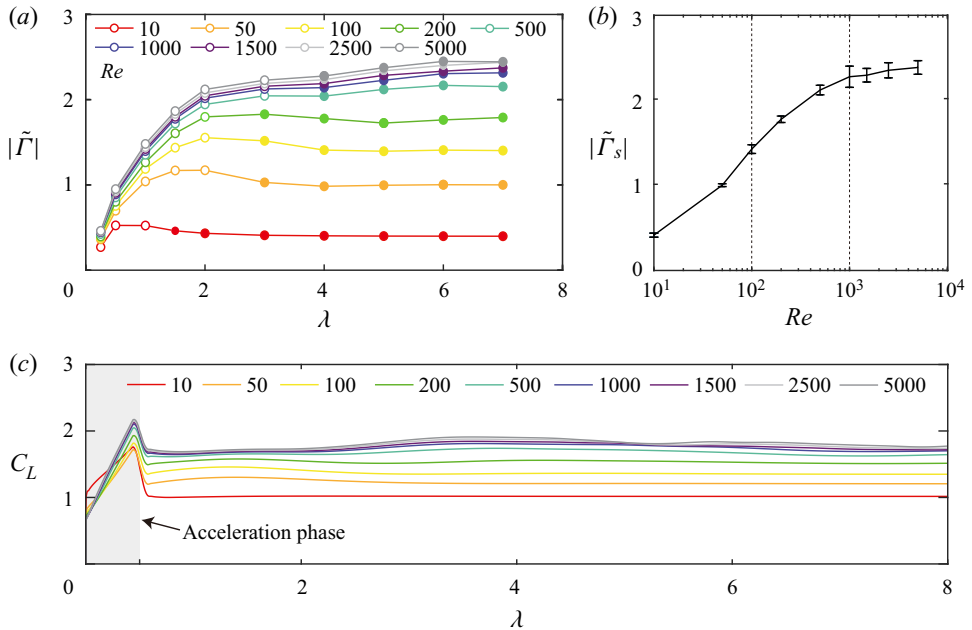


Figure 4. Effects of Re on LEV intensity and lift generation: (a) transient LEV intensity ($\tilde{\Gamma}$), (b) stable LEV intensity ($\tilde{\Gamma}_s$) and (c) transient lift coefficient (C_L). The solid symbols in panel (a) indicate that the LEV intensity is saturated, and the $\tilde{\Gamma}_s$ in panel (b) is calculated as the average of these solid dots with error bars denoting the standard deviations.

$\log_{10} Re$ is established within $Re < 500$. However, the $\tilde{\Gamma}_s$ plateaus when Re is above 500, indicating the existence of a limit for stable LEV intensity on revolving wings.

In addition, as shown in figure 4(c), the transient lift coefficients (C_L) at all Re almost reach their steady states by the end of acceleration, despite the fact that a slight fluctuation is observed at a Re higher than 1000. An increase of Re from 10 to 1000 leads to an enhancement of lift generation, which diminishes when Re is further increased.

Considering both transient and stable LEV intensity, it is evident that the effects of Re are stronger when Re is below 1000. To further elucidate the Re effects and understand the mechanisms behind the LEV formation and stability, we focus on the revolving wings at $Re = 10, 100$ and 1500 in the following sections. These Re are representative of those corresponding to the hovering flights of common insect species that have been studied, i.e. wasps, fruitflies and bees (table 1).

The evolution of 3-D vortical structure is shown in figure 5(a). At $Re = 1500$, a prominent vortex loop, including LEV, starting vortex, tip vortex and root vortex, is generated immediately after the start of the motion. During the steady state ($\lambda > 4$), the LEV is stable up to 63% span and an unsteady vortical region is observed near the tip. The stable LEV region is defined within the spanwise section where the LEV circulation remains approximately unchanged from $\lambda = 4$ (figure 5b). According to the vortical structure (figure 5a), the local LEV at the outboard limit of the stable LEV region, which is approximately 3, reaches the trailing edge, supporting the conclusions of Lentink & Dickinson (2009) and Jardin (2017). As Re decreases to 100, the vortical structure becomes steadier but less compact. Moreover, the stable LEV region is slightly enlarged and less unsteady vortical behaviour is seen around the tip. As Re further decreases to 10, the vortex ring remains attached to the rim and the LEV is stable along the entire span.

Re effects on LEV formation and stability in revolving wings

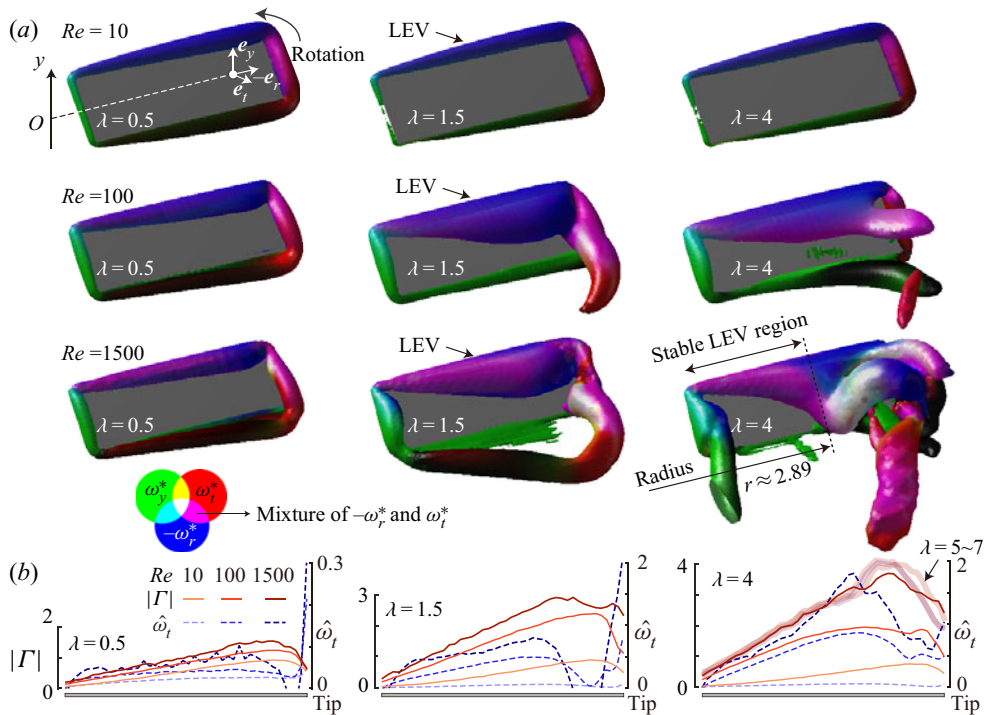


Figure 5. Effects of Re on LEV structure: (a) 3-D vortical structure (outlined by $Q = 2$) coloured by vorticity components and (b) spanwise distribution of LEV circulation and local tangential vorticity ($\hat{\omega}_t$). RGB values of the isosurface colour correspond to the magnitudes of vorticity components: ω_r^* , red; ω_y^* , green; and $-\omega_r^*$, blue.

When comparing vorticity components within the stable LEV region, a remarkable feature is that the LEV is a mixture of radial vorticity (ω_r^*) and tangential vorticity (ω_t^*), which is more apparent at $Re = 100$ and 1500 (see RGB colours in figure 5a). This mixing of ω_r^* and ω_t^* can result from the vortex tilting of radial vorticity components into the tangential direction.

The spanwise distributions of local LEV circulation (Γ) and tangential vorticity ($\hat{\omega}_t$) are shown in figure 5(b). Here, $\hat{\omega}_t$ is calculated by integrating the tangential vorticity within the LEV region. During the entire LEV formation, a linear increase of Γ along the span is observed for all three Re , except for the wing tip region, where the interaction of LEV and tip vortex breaks the linear trend. Moreover, the increase of Re leads to a stronger Γ at a certain radius and instant (λ). At $Re = 100$ and 1500 , the $\hat{\omega}_t$ also experiences a linear increase along the span and then drops near the wing tip. An increase of Re also enhances the strength of the tangential vorticity; however, no significant tangential vorticity is observed within the LEV at $Re = 10$. Note that the tangential vorticity near the tip can be negative during the LEV formation period ($\lambda = 1.5$ and 4), which is excluded from figure 4(b). The similar behaviours of Γ and $\hat{\omega}_t$ at $Re = 100$ and 1500 further suggest that radial vorticity and tangential vorticity may have coupled vorticity dynamics that are relevant to LEV stability.

3.2. Radial vorticity transport

To further evaluate the contributions of various mechanisms to the LEV formation and stability, a thorough analysis of radial vorticity transport is conducted. (A verification

of this quantitative analysis is provided in the supplementary material.) The analysis starts with an inspection of local convection and vortex tilting and stretching at different spanwise sections at $Re = 1500$ and 100 (referred to as ‘sectional analysis’, §§ 3.2.1 and 3.2.2), followed by a spatial–temporal analysis of vorticity transport terms within the entire Re range (§ 3.2.3, including viscous diffusion). Owing to the relatively simple structure and low intensity of the LEV, no sectional analysis is conducted at $Re = 10$.

3.2.1. Sectional analysis at $Re = 1500$

The convections of radial vorticity due to tangential and vertical flow (C_t and C_y) are observed after the onset of wing rotation, and their intensities increase until the steady state ($\lambda = 4$). As shown in figure 6(a), the downstream convection of negative radial vorticity ($C_t^{(+)}$ towards $C_t^{(-)}$) behind the leading edge feeds radial vorticity into the LEV. In addition, the downward convection of negative radial vorticity ($C_y^{(+)}$ towards $C_y^{(-)}$) behind the wing can further transport the LEV vorticity towards the trailing edge (figure 6b). Together, these convections prevent the LEV from continuously growing into the downstream direction and lead to its chord-aligned expansion. The downward convection of radial vorticity is also relevant to the tip-vortex-induced downwash effect (Birch & Dickinson 2001). For brevity, only steady-state C_t and C_y at $\lambda = 4$ are shown here since the only quantitative difference is observed during their formations towards the steady state. Note that these two vorticity convections become incoherent around the tip, which introduces strong unsteadiness into the evaluation of local LEV.

While the downstream and downward convection of radial vorticity might explain the primary source and drain of LEV vorticity, the saturation of LEV intensity should also be attributed to other vorticity transport mechanisms that continuously remove the radial vorticity of the LEV, leading to a dynamic equilibrium. One of the possible contributors is the radial (spanwise) convection of radial vorticity (C_r), which is shown in figure 6(c–f) for the LEV formation period. Two representative slices A and B are selected at $0.25b$ and $0.5b$, respectively, and a positive C_r ($C_r^{(+)}$) indicates tip-ward convection of negative radial vorticity. It is found that a strong $C_r^{(+)}$ transports the radial vorticity towards the tip during the entire LEV formation period. The region of this strong $C_r^{(+)}$ is initially extended beyond the mid-span (red tube-shaped region, figure 6c, A-i and B-i) but tends to be confined within the mid-span afterwards (figure 6d–f, A-i and B-i). Moreover, a significant $C_r^{(-)}$ region is observed where the LEV contacts the wing surface (especially around mid-span), indicating an enhancement of radial vorticity (blue region in figure 6c, B-i). Therefore, the integral of total C_r at the steady state is characterized by a reduction of radial vorticity near the wing root and a local enhancement around the mid-span ($\lambda > 4$). The $C_r^{(+)}$ in the inboard region, e.g. $0.25b$, is sustained under the steady state (figure 6d–f, A-i). Note that the chordwise $C_r^{(+)}$ region at a specific spanwise position is mostly located in the downstream boundary of the LEV (behind the local $C_r^{(-)}$ region). The spatial complexities of $C_r^{(+)}$ and $C_r^{(-)}$ in the LEV region are further elaborated in § 3.2.3. Note that no significant tip-ward vorticity convection is observed in the unsteady LEV region, i.e. outboard region beyond the mid-span, during the entire evolution.

To explain the behaviours of tip-ward vorticity convection, the evolution of spanwise flow, F_{pre} and F_{cor} , on two representative slices is discussed here (figure 6c–f, iii and iv). The F_{pre} and F_{cor} are examined here as possible driving forces of spanwise flow, whereas the contribution of centrifugal acceleration is ignored. This is because the centrifugal

Re effects on LEV formation and stability in revolving wings

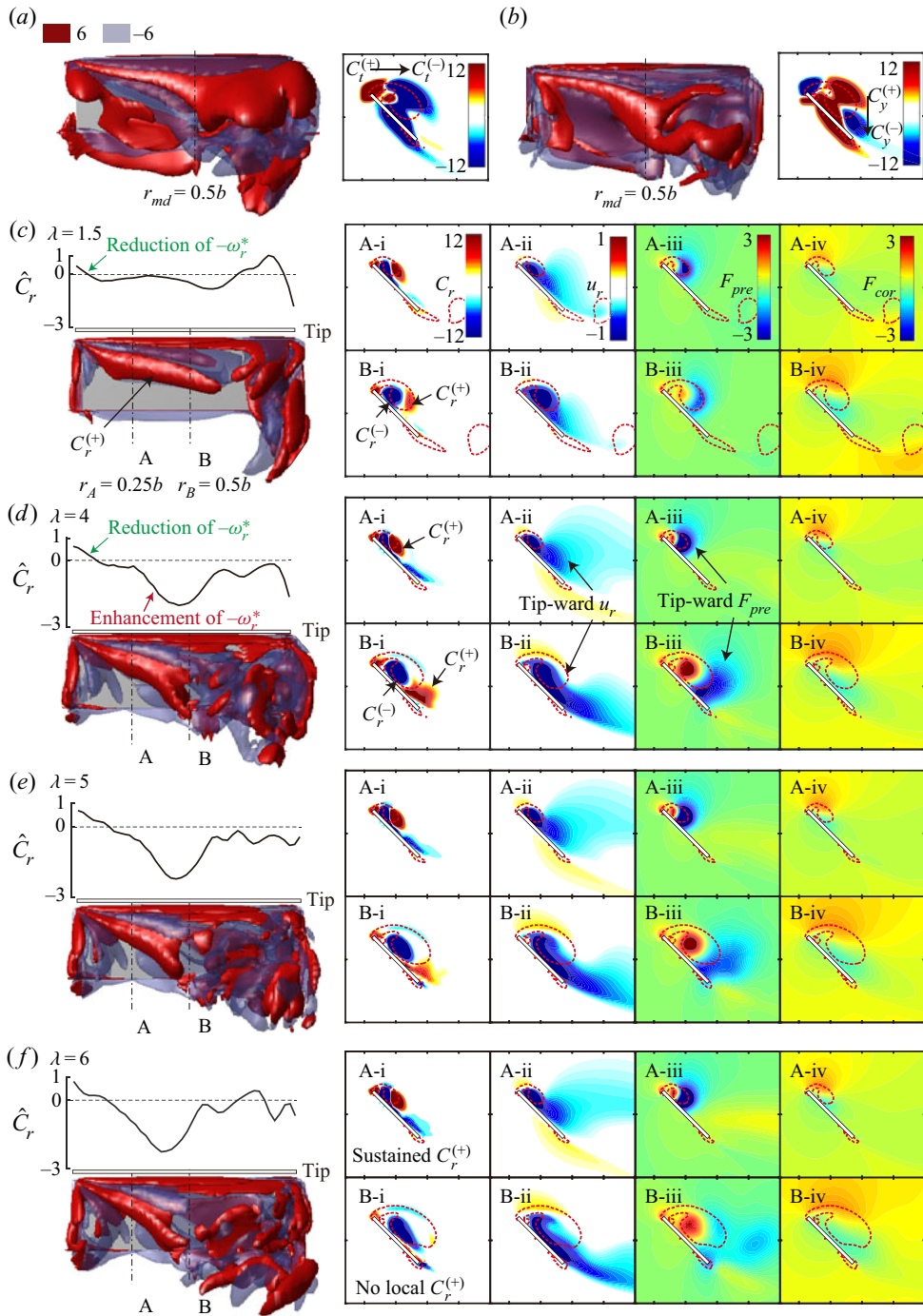


Figure 6. Convection of radial vorticity at $Re = 1500$: (a) steady-state tangential convection (C_r), (b) steady-state vertical convection (C_y), and (c–f) evolution of spanwise convection (C_r). The radial velocity (u_r), pressure gradient (F_{pre}) and Coriolis acceleration (F_{cor}) on two representative cylindrical slices A and B ($0.25b$ and $0.5b$) are shown in panels i to iv, with the vortical region circled by $Q = 1$. Here, \hat{C}_r is the integral of C_r within the LEV region.

acceleration is weaker than the pressure gradient and Coriolis acceleration and remains constant within the cylindrical slice at $0.25b$ or $0.5b$. In addition, since the strong spanwise flow is mostly located above the upper surface of the wing (figure 6c–f, A-ii), the F_{pre} and F_{cor} , instead of the centrifugal acceleration, are more likely to be responsible for the formation of spanwise flow. It can be observed that a strong spanwise flow exists within the LEV at $0.25b$ (figure 6c–f, A-ii) and extends into the wake and covers the entire dorsal surface of the wing at $0.5b$ (figure 6c–f, B-ii).

Moreover, an apparent tip-ward pressure gradient (F_{pre}) exists near the downstream edge of the LEV at $0.25b$ (figure 6c–f, A-iii), overlapped with regions of the local spanwise flow. However, the F_{pre} inside the LEV is reversed at $0.5b$ and the local tip-ward F_{pre} region becomes dispersed behind the LEV (figure 6c–f, B-iii). The contribution of F_{cor} in the formation of spanwise flow is significantly weaker than that of F_{pre} , although the tip-ward F_{cor} region shows a good agreement with the local tip-ward spanwise flow at both $0.25b$ and $0.5b$ (figure 6c–f, A-iv and B-iv). Comparing the regions of $C_r^{(+)}$ and F_{pre} , it is remarkable that $C_r^{(+)}$ regions can be well predicted by those of tip-ward F_{pre} at both $0.25b$ and $0.5b$, which suggests that the reduction of $C_r^{(+)}$ around the mid-span (beyond which LEV becomes less stable) can be attributed to the lack of tip-ward pressure gradient. Therefore, despite the fact that the tip-ward spanwise flow is usually considered as a source of tip-ward vorticity convection (Ellington *et al.* 1996; Wu & Sun 2004), our result suggests that the tip-ward vorticity convection is strongly related to the establishment of tip-ward pressure gradient.

Apart from convections of radial vorticity, the vortex tilting and stretching also contribute to the LEV stability. We examined the vortex tilting and stretching at two representative slices at $Re = 1500$ (figure 7, slices A and B), including a decomposition into four components (panels i to iv showing $T_{t \rightarrow r}$, $T_{y \rightarrow r}$, PVT_r and S_r , respectively). The integrals of vortex tilting and stretching within the LEV region are plotted over the span (i.e. $\hat{T}_{t \rightarrow r}$, \widehat{PVT}_r and \hat{S}_r). The overall contribution of vortex tilting and stretching can balance the LEV vorticity around the mid-span (first column in figure 7b–d). When separating into individual components, the $T_{t \rightarrow r}$ and PVT_r are dominated by their positive subterms ($T_{t \rightarrow r}^{(+)}$ and $PVT_r^{(+)}$) in the LEV region and consistently remove LEV vorticity within the mid-span (second and fourth columns in figure 7b–d).

Among all vortex tilting and stretching in the radial direction, $T_{t \rightarrow r}$ has the strongest intensity and occurs within the entire half-span from the root ($\hat{T}_{t \rightarrow r}$ in figure 7a–d). The contribution of PVT_r remains consistent along the entire span but at a considerably lower magnitude (\widehat{PVT}_r in figure 7a–d). Moreover, PVT_r exhibits low spatial–temporal variations, indicating that it is a consistent mechanism removing LEV vorticity during both the formation period and steady state. In contrast, the evolution of S_r is more complex. The \hat{S}_r at $0.25b$ indicates a vortex stretching (enhancement) of radial vorticity during the LEV formation (A-iv in figure 7a–d) whereas a strong vortex compression (removal) of radial vorticity is observed around the mid-span during $\lambda = 4–6$ (B-iv in figure 7b–d). From the \hat{S}_r in figure 7, the peak of vortex compression is generated around the wing tip at $\lambda = 1.5$ and then moves towards the mid-span until the steady state. This inward movement of \hat{S}_r peak can compensate for the local reduction of tip-ward vorticity convection (figure 6d–f), and thus helps to remove the local LEV vorticity.

From above, $T_{t \rightarrow r}$ is one of the most important contributors to LEV stability at $Re = 1500$. On the other hand, the vortex tilting from radial vorticity into the tangential direction ($T_{r \rightarrow t}$), as indicated by the 3-D LEV structure in figure 5(a), contributes to the

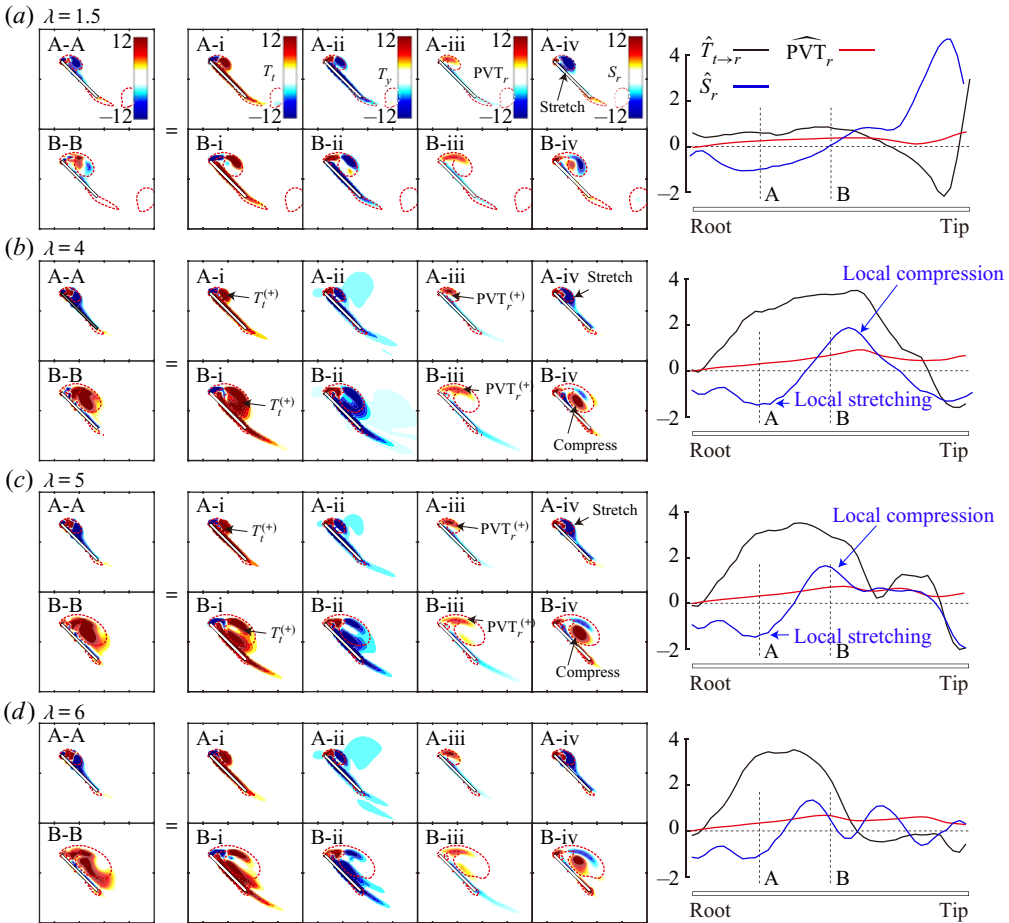


Figure 7. Vortex tilting and stretching in the radial direction at $Re = 1500$: (a) $\lambda = 1.5$, (b) $\lambda = 4$, (c) $\lambda = 5$ and (d) $\lambda = 6$. The representative slices A and B are defined in figure 6. Here, $\hat{T}_{t \rightarrow r}$, \widehat{PVT}_r and \hat{S}_r are the integrals of $T_{t \rightarrow r}$, PVT_r and S_r within the LEV region.

development of tangential vorticity. Thus, the tangential vorticity transport terms within the LEV are examined. Here, the convection of tangential vorticity is omitted and only the tangential components of vortex tilting in (2.7), including $T_{r \rightarrow t}$, $T_{y \rightarrow t}$ and PVT_t , are discussed. Since the tangential vorticity within the LEV is mostly positive (figure 8a), positive values of $T_{r \rightarrow t}$, $T_{y \rightarrow t}$ and PVT_t , i.e. $T_{r \rightarrow t}^{(+)}$, $T_{y \rightarrow t}^{(+)}$ and $PVT_t^{(+)}$, indicate an increase of local tangential vorticity. As shown in figure 8(a), $T_{r \rightarrow t}^{(+)}$ and $PVT_t^{(+)}$ tend to enhance the tangential vorticity in the inboard region. In the outboard region, $PVT_t^{(+)}$ is the main source that enhances local tangential vorticity. According to the derivation of Werner *et al.* (2019), the PVT_t is mathematically related to the vertical gradient of radial Coriolis acceleration. Thus, the radial Coriolis acceleration is found to be strongly related to the increase of tangential vorticity.

According to the $T_{t \rightarrow r}^{(+)}$ and $T_{r \rightarrow t}^{(+)}$ shown in figures 7 and 8, there exists a conversion between radial vorticity and tangential vorticity within the mid-span, resembling a negative feedback loop that stabilizes the vorticity in both directions. When the local radial vorticity (tip-ward) accumulates, the local tangential vorticity also increases via induced

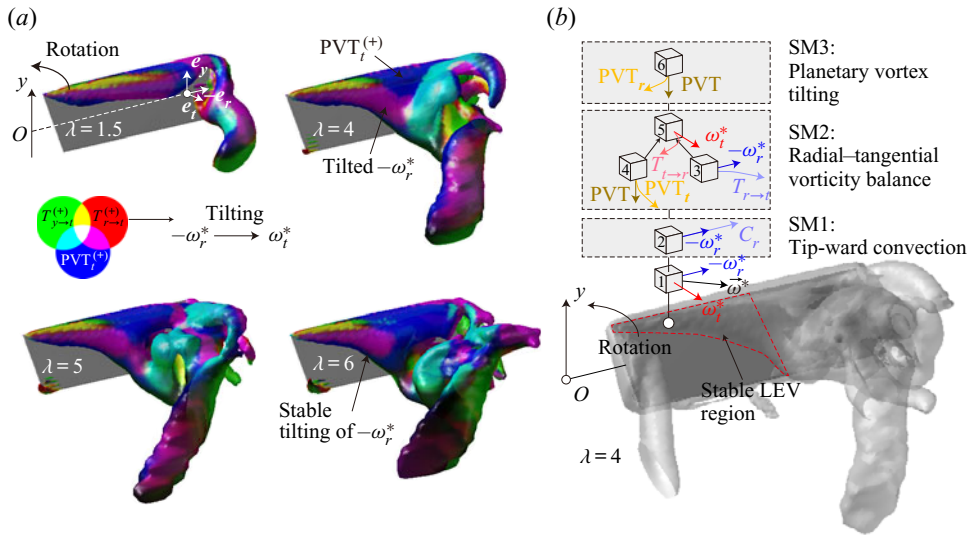


Figure 8. The balance of radial and tangential vorticity at $Re = 1500$. (a) Vortex tilting in the evolution of tangential vorticity and (b) a schematic of primary stabilizing mechanisms (SMs) in the stable LEV region. The isosurfaces are drawn by $\omega_t^* = 2$ and $Q = 2$.

vortex tilting ($T_r^{(+)}$). This further enhances the vortex tilting of tangential vorticity into the positive radial direction ($T_t^{(+)}$), which is opposite to the radial vorticity in the LEV. This conversion functions as a negative feedback loop that attenuates the increase of local tip-ward radial vorticity, leading to a dynamic equilibrium, i.e. a steady state. Therefore, it is likely that the stable LEV in the inboard region can be mainly attributed to this mechanism, which we name as ‘radial–tangential vorticity balance’ (RTVB). In summary, the stable LEV in the inboard region at $Re = 1500$ is mainly led by three stabilizing mechanisms (SMs), including tip-ward vorticity convection, RTVB and planetary vorticity tilting (figure 8b). In terms of the intensity of these SMs, the RTVB contributes most to the inboard LEV stability (see $T_t^{(+)}$ in figure 7). It should be noted that the tangential tilting of planetary vorticity, which is related to the radial Coriolis acceleration, is one of the main sources of tangential vorticity, and therefore also contributes towards the LEV stability, albeit indirectly, via the RTVB mechanism. The RTVB and the PVT_r are sustained within the entire stable LEV region whereas the tip-ward vorticity convection becomes diminished around the mid-span at the steady state (figure 6). The local reduction of tip-ward vorticity convection around mid-span is compensated by the increase of vortex compression of radial vorticity (figure 7).

3.2.2. Sectional analysis at $Re = 100$

As Re decreases to 100, the stable LEV region is extended towards the wing tip while the conical LEV structure becomes less compact (figure 5a). Meanwhile, the strength of most vorticity transport terms (except PVT_r) is reduced. As shown in figure 9, the tangential convection and the vertical convection (C_t and C_y) resemble their counterparts at $Re = 1500$, whereas the 3-D structures become more stable (figure 9a,b). Moreover, the tip-ward vorticity convection is also present (outlined by the positive C_r , i.e. $C_r^{(+)}$), in figure 9c–e) and therefore contributes to LEV stability at $Re = 100$. However, while the $C_r^{(+)}$

region extends beyond the mid-span during LEV formation, it becomes more confined towards $0.25b$ at the steady state (figure 9e). Moreover, the spanwise flow (tip-ward) covers most of the dorsal wing surface at $Re = 100$, which is not well overlapped with the LEV region (figure 9c–e, A-ii and B-ii). Note that an apparent tip-ward spanwise flow is formed at the mid-span whereas less local tip-ward vorticity convection is observed (figure 9c–e). Similar to the $Re = 1500$ case, the $C_r^{(+)}$ region can also be mostly predicted by that of tip-ward pressure gradient (F_{pre}) at $Re = 100$. For the generation of spanwise flow, the contributions of F_{pre} and radial Coriolis acceleration (F_{cor}) are comparable. Since the tip-ward F_{cor} region shows a good agreement with tip-ward spanwise flow, it can be inferred that the spanwise flow at $Re = 100$ is mainly driven by radial Coriolis acceleration, the mechanism of which is akin to the Ekman pump as described by Lentink & Dickinson (2009).

The evolution of vortex tilting and stretching is further examined at $Re = 100$ (figure 10). Note that the results at $\lambda = 0.5$ are insignificant and are not shown here. As Re decreases to 100, $T_{t \rightarrow r}^{(+)}$ and $PVT_r^{(+)}$ become the two dominant vorticity transport mechanisms that contribute to LEV stability (figure 10b,c). Unlike the $Re = 1500$ case, the intensity of $PVT_r^{(+)}$ is now stronger than that of $T_{t \rightarrow r}^{(+)}$ within the LEV (shown by $\hat{T}_{t \rightarrow r}$ and \widehat{PVT}_r). The LEV vorticity at $0.25b$ is mainly removed by $PVT_r^{(+)}$ while both $T_{t \rightarrow r}^{(+)}$ and $PVT_r^{(+)}$ contribute to LEV stability at $0.5b$. When comparing \widehat{PVT}_r at $Re = 100$ and 1500 (figures 7 and 10), it is found that the intensity and spanwise distribution of \widehat{PVT}_r remain almost identical as Re decreases, indicating that the contribution of PVT_r in LEV stability is almost Re -independent.

To further examine the Re dependence of the RTVB mechanism, the temporal variation of tangential vorticity and the contribution of vortex tilting at $Re = 100$ are shown in figure 11. Since the vortex stretching becomes negligible at $Re = 100$ (figure 10), no discussion on vortex stretching is presented here. It is shown that the vortex tilting from radial vorticity into the tangential direction ($T_{r \rightarrow t}^{(+)}$) exists in the entire LEV region during its formation ($\lambda < 2$) and stabilizes within the inboard region at the steady state. Together with the strong $T_{t \rightarrow r}^{(+)}$ shown in figure 10, it can be seen that the RTVB mechanism also contributes to the LEV stability at $Re = 100$. Moreover, the PVT_t , which is related to the radial Coriolis acceleration, contributes consistently towards the development of tangential vorticity at both $Re = 100$ and 1500. In summary, as Re decreases to 100, the three SMs illustrated in figure 8(b) still all contribute to the inboard LEV stability, but with varied relative magnitudes. The tip-ward vorticity convection (SM1) and the RTVB (SM2) are significantly reduced in strength at $Re = 100$, while the intensity and distribution of the radial tilting of planetary vorticity (SM3) are almost Re -independent between $Re = 100$ and 1500.

3.2.3. Discussion on the spatial distribution of spanwise convection and vortex stretching

According to our sectional analysis, the overall integrals of $T_{t \rightarrow r}$ and PVT_r are dominated by, and therefore can be represented by, their positive subterms $T_{t \rightarrow r}^{(+)}$ and $PVT_r^{(+)}$. (Integrals of $T_{t \rightarrow r}^{(-)}$ and $PVT_r^{(-)}$ are available in the supplementary material). However, the spanwise convection and vortex stretching have more complex spatial distributions with positive and negative subterms occupying distinct regions within the LEV. Thus, here we express \hat{C}_r and \hat{S}_r as the sum of two sub-integrals, i.e. $\hat{C}_r = \hat{C}_r^+ + \hat{C}_r^-$, where

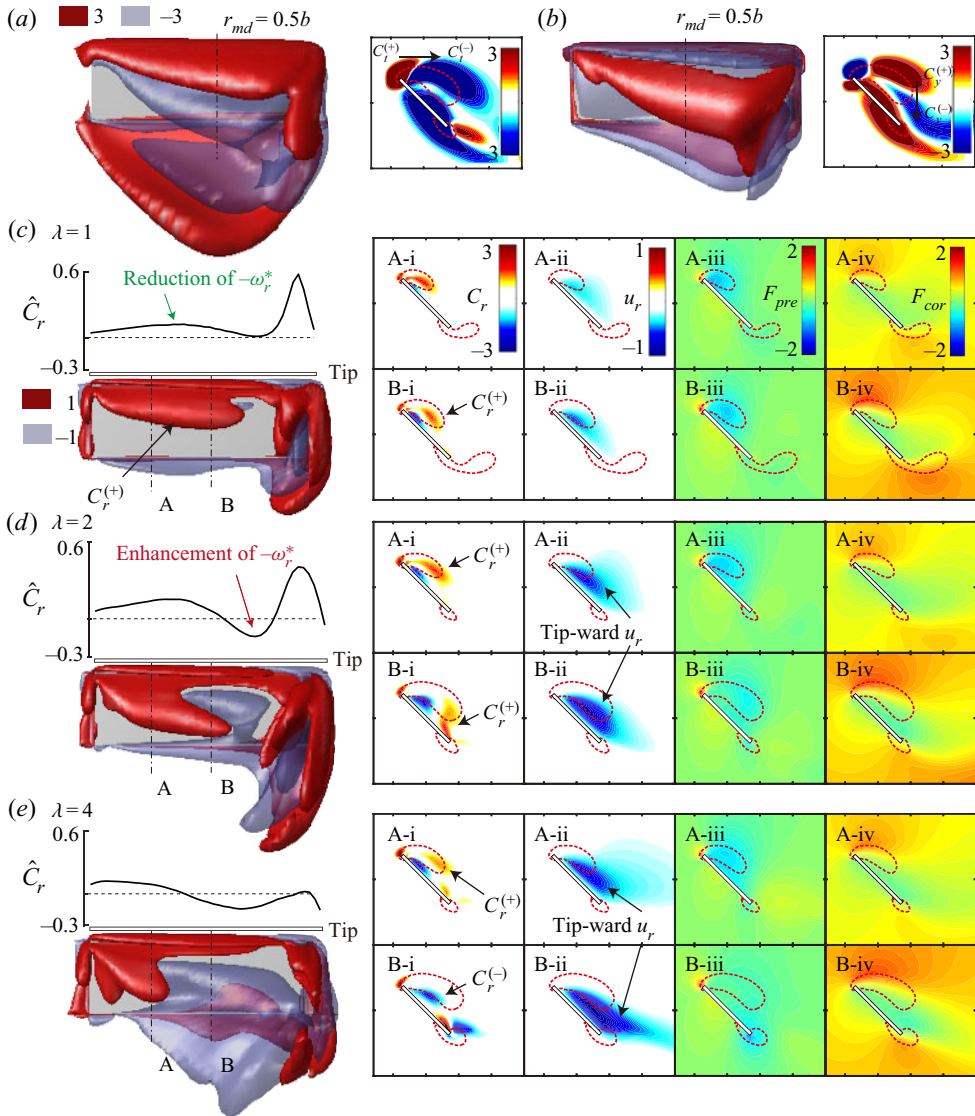


Figure 9. Convection of radial vorticity at $Re = 100$: (a) steady-state C_r , (b) steady-state C_y and (c–e) evolution of C_r . Details about the various panels can be found in figure 6.

\hat{C}_r^+ and \hat{C}_r^- denote the integrals of positive and negative subterms of C_r within the LEV. As shown in figure 12(a), the \hat{C}_r^+ peaks are located at around 25% span at the steady state (region I) while the \hat{C}_r^- peaks are shifted towards the mid-span (region II). Moreover, the \hat{C}_r^- peaks are stronger than those of \hat{C}_r^+ , thus leading to the negative sign of total \hat{C}_r shown in figure 6. According to the 3-D structures in figure 12(a) and representative slices in figure 6(c–f), the $C_r^{(+)}$ is mostly located behind the $C_r^{(-)}$ and near the downstream boundary of the LEV. This indicates that the radial vorticity can maintain a better attachment near the leading edge since the $C_r^{(-)}$ region is closer to the

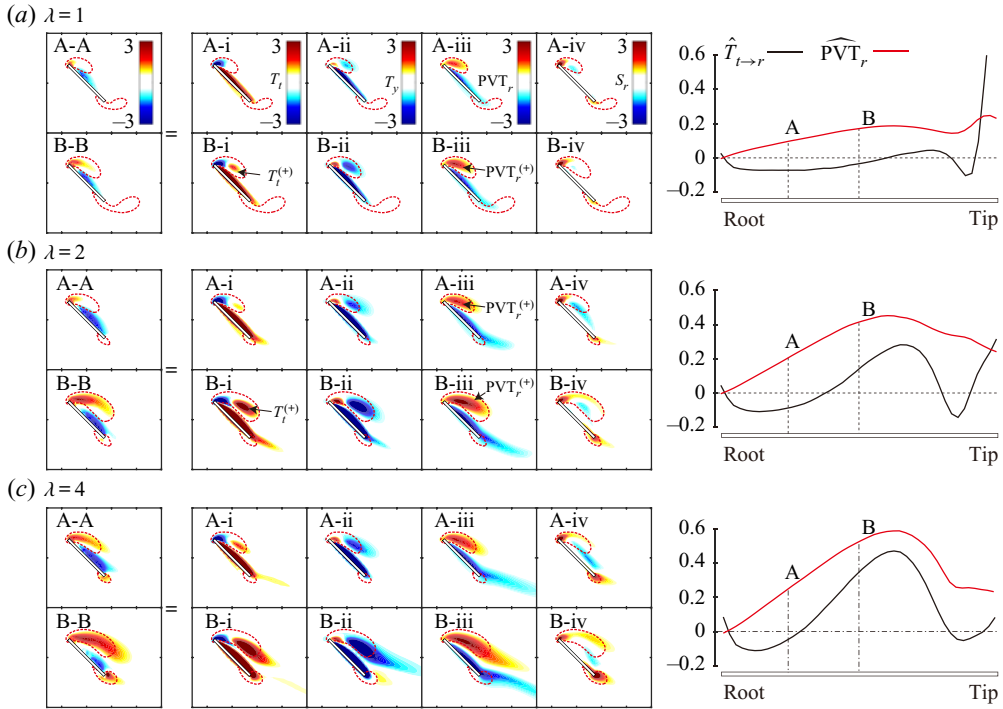


Figure 10. Vortex tilting and stretching in the radial direction at $Re = 100$: (a) $\lambda = 1$, (b) $\lambda = 2$ and (c) $\lambda = 4$. The representative slices A and B are defined in figure 9.

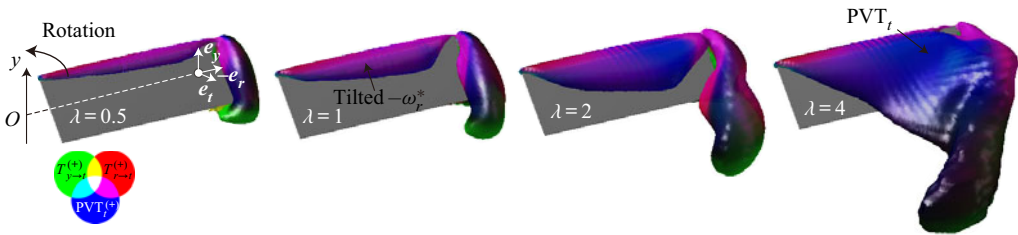


Figure 11. Vortex tilting in the evolution of tangential vorticity at $Re = 100$. The isosurface is drawn by $\omega_t^* = 1$.

wing surface. Note that the \hat{C}_r^+ and \hat{C}_r^- experience a similar behaviour at $Re = 100$ (shown in the supplementary material).

In figure 12(b), the separation of \hat{S}_r^+ and \hat{S}_r^- shows that the steady-state S_r are dominated by positive subterms (compression) beyond the mid-span, although there can be multiple peaks of \hat{S}_r^+ at $\lambda = 6$. The \hat{S}_r^+ is developed from the wing tip and then spreads towards the inboard region (see region I of 3-D structures). In contrast, the steady-state S_r in the inboard region mainly results in a vortex stretching effect, which enhances the local radial vorticity (region II). According to the representative slices in figure 8, the mid-span $S_r^{(+)}$ is located around the core of the LEV whereas the local $S_r^{(-)}$ is at the top of the LEV (and with a weaker intensity). Therefore, the contribution of S_r in LEV stability at

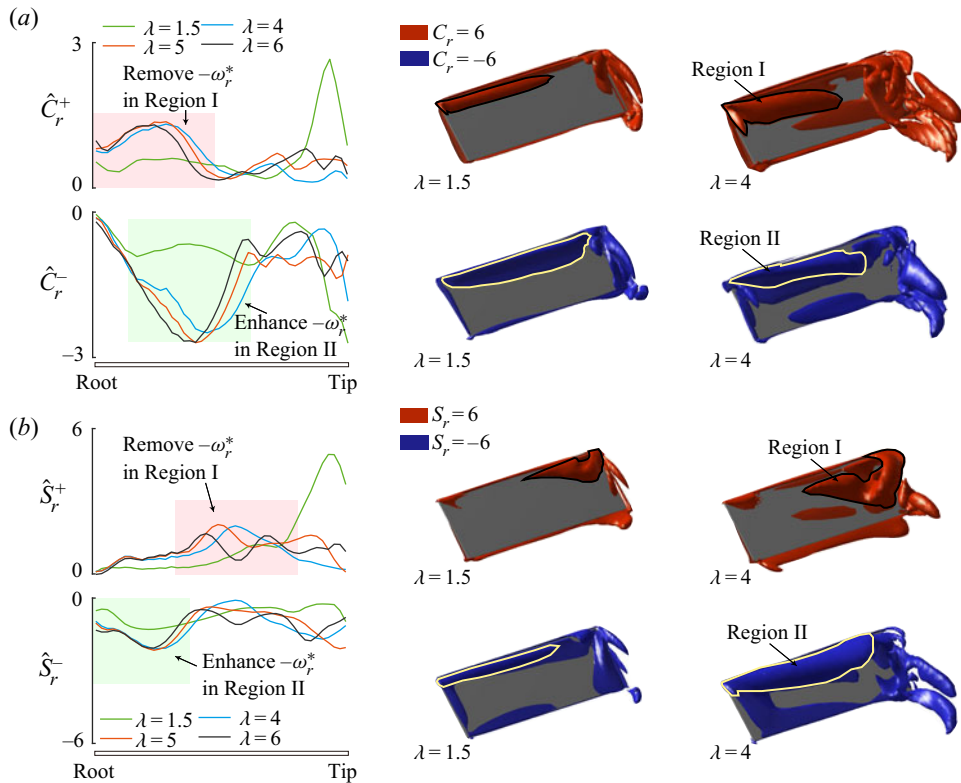


Figure 12. Positive and negative subterms of spanwise convection and vortex stretching in the LEV region at $Re = 1500$: (a) spanwise convection and (b) vortex stretching.

$Re = 1500$ depends on the spanwise location, and a switch from vortex stretching to vortex compression occurs around the mid-span.

3.2.4. Mechanisms contributing to LEV stability: a spatial–temporal analysis

The spatial–temporal variation of primary vorticity convection and vortex tilting and stretching terms at varying Re is summarized in figure 13. Five representative slices are presented to demonstrate the spatial variation along the span, and the integrals of positive subterms in C_r , $T_{t \rightarrow r}$, PVT_r and S_r , i.e. \hat{C}_r^+ , $\hat{T}_{t \rightarrow r}^+$, \widehat{PVT}_r^+ and \hat{S}_r^+ , are considered here. First, it is evident that the radial tilting of planetary vorticity (\widehat{PVT}_r^+) not only is almost Re -independent (when Re is higher than 100) but also has the least spatial (spanwise) and temporal variations when fully developed (figure 13c). In contrast, tip-ward vorticity convection (\hat{C}_r^+) is mostly confined within the mid-span and becomes stronger when $Re > 1000$ (figure 13a). Note that the strong \hat{C}_r^+ at $0.9b$ is attributed to the interaction with the tip vortex. At $Re > 1000$, \hat{C}_r^+ beyond the mid-span (at the steady state) is absent while vortex compression (\hat{S}_r^+ in figure 13d) assists in stabilizing the local LEV. Once the Re is below 100, the \hat{C}_r^+ and \hat{S}_r^+ are both negligible.

The Re effect on the radial tilting of tangential vorticity (shown by $\hat{T}_{t \rightarrow r}^+$) is strong and there is a steep reduction of intensity as Re decreases from 500 to 100 (figure 13b). The main $\hat{T}_{t \rightarrow r}^+$ region is mostly located within the mid-span at $Re > 1000$. The RTVB

Re effects on LEV formation and stability in revolving wings

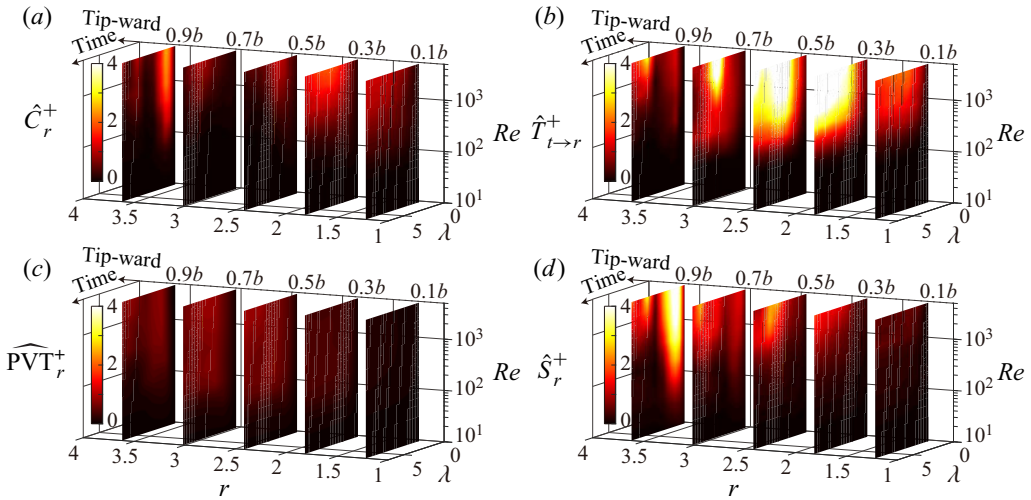


Figure 13. The effects of Re on the spatial–temporal evolution of vorticity convection, vortex tilting and stretching that contribute to LEV stability: (a) \hat{C}_r^+ , (b) $\hat{T}_{t \rightarrow r}^+$, (c) \widehat{PVT}_r^+ and (d) \hat{S}_r^+ .

illustrated in figure 8 is related to this strong $\hat{T}_{t \rightarrow r}^+$. Consequently, the inboard LEV stability of revolving wings at $Re > 1000$ can be mainly attributed to the tip-ward vorticity convection, RTVB and the radial tilting of planetary vorticity, despite the fact that the vortex compression also contributes to LEV stability near mid-span. For Re around 100, the radial tilting of planetary vorticity and RTVB become the two main mechanisms.

As Re further decreases to 10, the effects of vorticity convection and vortex tilting and stretching in LEV formation and stability become negligible (which can be inferred from figure 13), indicating that the vorticity generated from the leading edge remains close to the rim. Therefore, the 3-D LEV structure at $Re = 10$ is closely aligned with the leading edge and no conversion of radial vorticity and tangential vorticity is observed (figure 5a). In our following discussion, it is found that viscous diffusion (D in (2.9)) regulates the increase of radial vorticity within the LEV at $Re = 10$. The positive viscous diffusion within the LEV region is integrated (\hat{D} in figure 14a) and a linear increase of \hat{D} over the span is observed at both $Re = 10$ and 100. The viscous diffusion in the LEV region is reduced as Re increases and becomes almost negligible at $Re > 1000$. According to a spatial–temporal analysis of integrated viscous diffusion within the LEV, i.e. \tilde{D} (figure 14b), the contribution of viscous diffusion in LEV stability is comparable to the PVT_r and RTVB when Re is about 200 (the legends of figures 13 and 14 are identical). For revolving wings with $Re < 200$, the viscous diffusion starts to dominate the evolution of radial vorticity. Since other vorticity transport mechanisms are almost negligible at $Re = 10$, the conical LEV structure at this Re level is maintained under the balance of vorticity shedding from the leading edge and viscous diffusion. Note that the \tilde{D} can experience a transient overshoot at the end of acceleration ($\lambda = 0.5$) at $Re < 100$, as shown by the star in figure 14(b).

3.3. Re effects on the mechanisms of LEV stability

Based on the above analyses, the primary mechanisms of LEV stability are strongly Re -dependent. For a revolving wing at extremely low Re , e.g. $Re = 10$, no vorticity convection, vortex tilting and stretching are observed over the LEV formation.

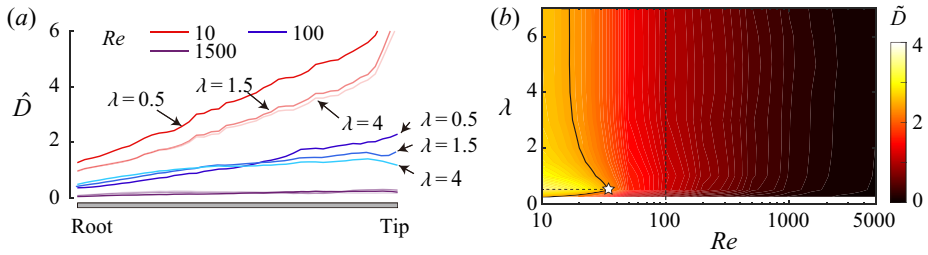


Figure 14. The effects of Re on viscous diffusion within the LEV region: (a) spanwise distribution and (b) spatial-temporal analysis. The plain line in figure 13(b) shows the contour line at $\hat{D} = 2.5$.

The vorticity generated at the leading edge accumulates around the rim and is regulated by strong viscous diffusion, thus leading to a stable LEV. The contribution of viscous diffusion on LEV stability is dominant until Re increases to 200 (figure 14b), when vortex tilting becomes comparable (figure 13b,c). The vortex tilting includes the tilting of planetary vorticity (PVT_r) and the tilting of tangential vorticity into the radial direction ($T_{t \rightarrow r}$). The PVT_r was first proposed by Werner *et al.* (2019, 2020) and a close relationship between PVT_r and tangential Coriolis acceleration was elucidated in their work. The $T_{t \rightarrow r}$ together with the tilting from radial vorticity into the tangential direction ($T_{r \rightarrow t}$) establish a dynamic two-step balance between radial vorticity and tangential vorticity, i.e. RTVB. This novel mechanism resembles a negative feedback loop with the two-step balance as the feedback path that regulates the LEV vorticity. Notably, both $T_{t \rightarrow r}$ and $T_{r \rightarrow t}$ stem from the nature of revolving motion, since the former contains the tangential gradient of radial velocity ($\partial u_r^* / \partial t$) and the latter contains the radial gradient of tangential velocity ($\partial u_t^* / \partial r$), respectively. The first step in conversion of RTVB (or the first step of the analogous feedback path) refers to the tilting of negative radial vorticity into the positive tangential direction, while the second step refers to the tilting of positive tangential vorticity back into the positive radial vorticity, and therefore forms a negative feedback path. As a result, any increase of local radial vorticity in the LEV can be regulated, at least partially, by this feedback loop.

For scenarios at higher Re , e.g. $Re = 1000$, the contribution of viscous diffusion in LEV stability is negligible, while vortex tilting, as well as tip-ward vorticity convection and vortex compression, are the main mechanisms that contribute to LEV stability. The intensity of $T_{t \rightarrow r}$ is significantly enhanced as Re increases and contributes most to removing the LEV vorticity (figure 13b). The second important mechanism for LEV stability at $Re = 1000$ is the tip-ward vorticity convection ($C_r^{(+)}$), which is also intensified but shrinks in its region towards the wing root as Re increases to 1000 (figure 13a). The region of $C_r^{(+)}$ does not overlap well with the spanwise flow region; however, it does overlap well with regions of strong tip-ward pressure gradient (figures 6 and 9). Although the tip-ward vorticity convection becomes almost absent around the mid-span at the steady state, a local peak of vortex compression in this region can alternatively help in removing the local LEV vorticity (figure 13d). In addition, except for viscous diffusion, the PVT_r contributes the least to the LEV stability at $Re > 1000$. This is because $T_{t \rightarrow r}$ and $C_r^{(+)}$ become more dominant at a higher Re , while the contributions of PVT_r remain approximately unchanged.

Our findings support previous studies that emphasize the importance of tip-ward vorticity convection (Ellington *et al.* 1996; Wu & Sun 2004; Shyy & Liu 2007; Lentink & Dickinson 2009) and planetary vorticity tilting (Werner *et al.* 2019) in LEV stability.

Also, Jardin (2017) points out that the LEV is stabilized under viscous effects at $Re < 200$, which is also supported by our findings. It should be noted that the AR and root cutoff are fixed in our research. According to Lentink & Dickinson (2009) and Jardin & Colonius (2018), variations of AR and root cutoff can shift the stable LEV region and therefore potentially alter the underlying vorticity dynamics. This will be the focus of our subsequent research.

4. Conclusions

The effects of Reynolds number (Re) on leading-edge vortex (LEV) formation dynamics and stability in revolving wings are numerically studied with Re varying from 10 to 5000. The aspect ratio and the angle of attack of the wing are fixed at 45° and a constant angular acceleration is prescribed within the first 0.5 chord lengths of travel at the radius of gyration, followed by a constant speed revolving. An in-house solver is employed to simulate the unsteady flow, which is further analysed via the vorticity transport equation in a co-rotating frame.

Our results show that, as Re decreases from 1000 to 10, the critical chord length of travel for the formation of steady-state LEV and its intensity are both reduced. For revolving wings with $Re < 100$, the LEV, which is mainly regulated by viscous diffusion, is attached to the wing edges instead of moving into the wake. The contribution of viscous diffusion in stabilizing LEV becomes negligible at $Re > 200$ when vortex tilting becomes the primary contributor to LEV stability.

The vortex tilting includes two major mechanisms, i.e. the planetary vorticity tilting and the tilting from tangential vorticity to radial vorticity. The latter, together with the tilting from radial vorticity to tangential vorticity, introduces a dynamic two-step balance of vorticity in both directions, which is considered as a novel mechanism, named as the radial–tangential vorticity balance (RTVB). As Re further increases above 1000, apart from vortex tilting, tip-ward vorticity convection and vortex compression also contribute to stabilizing local LEV within the mid-span. The effective region of tip-ward vorticity convection, which overlaps well with those of tip-ward pressure gradient, first exceeds the mid-span during LEV formation and then shrinks towards the wing root at steady state. Although the intensity of RTVB and tip-ward vorticity convection both increase with Re , the planetary vorticity tilting has relatively small variation, therefore having a Re -independent contribution to LEV stability.

Our findings support previous hypotheses on LEV stability with the addition of a novel mechanism of vortex tilting. This work also presents a comprehensive assessment of the spatial–temporal contributions of these mechanisms to LEV stability, and their Re dependence. Together, this work provides novel insights towards the LEV formation and stability on low- Re revolving wings.

Supplementary material. Supplementary material is available at <https://doi.org/10.1017/jfm.2021.950>.

Acknowledgements. The authors would like to thank N.H. Werner at Pennsylvania State University for his discussion on the leading-edge vortex dynamics.

Funding. This research was financially supported by the National Natural Science Foundation of China (NSFC, grant numbers 12002082 and 11902017), the China Postdoctoral Science Foundation (grant number 2019M661110), the Fundamental Research Funds for the Central Universities (grant number 2005002), and the Postdoctoral Research Fund of Northeastern University.

Declaration of interests. The authors report no conflict of interest.

Author ORCIDs.

Long Chen <https://orcid.org/0000-0002-0222-2665>;

Bo Cheng <https://orcid.org/0000-0002-6982-0811>.

REFERENCES

- BHAT, S.S., ZHAO, J., SHERIDAN, J., HOURIGAN, K. & THOMPSON, M.C. 2019a Aspect ratio studies on insect wings. *Phys. Fluids* **31** (12), 121301.
- BHAT, S.S., ZHAO, J., SHERIDAN, J., HOURIGAN, K. & THOMPSON, M.C. 2019b Uncoupling the effects of aspect ratio, Reynolds number and Rossby number on a rotating insect-wing planform. *J. Fluid Mech.* **859**, 921–948.
- BIRCH, J.M. & DICKINSON, M.H. 2001 Spanwise flow and the attachment of the leading-edge vortex on insect wings. *Nature* **412** (6848), 729–733.
- BIRCH, J.M., DICKSON, W.B. & DICKINSON, M.H. 2004 Force production and flow structure of the leading edge vortex on flapping wings at high and low Reynolds numbers. *J. Expl Biol.* **207** (7), 1063–1072.
- CARR, Z.R., DEVORIA, A.C. & RINGUETTE, M.J. 2015 Aspect-ratio effects on rotating wings: circulation and forces. *J. Fluid Mech.* **767**, 497–525.
- CHEN, L., WU, J. & CHENG, B. 2019 Volumetric measurement and vorticity dynamics of leading-edge vortex formation on a revolving wing. *Exp. Fluids* **60** (1), 12.
- CHEN, L., WU, J. & CHENG, B. 2020 Leading-edge vortex formation and transient lift generation on a revolving wing at low Reynolds number. *Aerosp. Sci. Technol.* **97**, 105589.
- CHEN, L., WU, J., ZHOU, C., HSU, S.-J. & CHENG, B. 2018 Unsteady aerodynamics of a pitching-flapping-perturbed revolving wing at low Reynolds number. *Phys. Fluids* **30** (5), 051903.
- CHENG, B., SANE, S.P., BARBERA, G., TROOLIN, D.R., STRAND, T. & DENG, X. 2013 Three-dimensional flow visualization and vorticity dynamics in revolving wings. *Exp. Fluids* **54** (1), 1423.
- CHENG, X. & SUN, M. 2016 Wing-kinematics measurement and aerodynamics in a small insect in hovering flight. *Sci. Rep.* **6**, 25706.
- DICKINSON, M.H. & GOTZ, K.G. 1993 Unsteady aerodynamic performance of model wings at low Reynolds numbers. *J. Expl Biol.* **174** (1), 45–64.
- DICKINSON, M.H., LEHMANN, F.-O. & SANE, S.P. 1999 Wing rotation and the aerodynamic basis of insect flight. *Science* **284** (5422), 1954–1960.
- ELLINGTON, C.P., VAN DEN BERG, C., WILLMOTT, A.P. & THOMAS, A.L.R. 1996 Leading-edge vortices in insect flight. *Nature* **384** (6610), 626–630.
- GARMANN, D.J. & VISBAL, M.R. 2014 Dynamics of revolving wings for various aspect ratios. *J. Fluid Mech.* **748**, 932–956.
- GARMANN, D.J., VISBAL, M.R. & ORKWIS, P.D. 2013 Three-dimensional flow structure and aerodynamic loading on a revolving wing. *Phys. Fluids* **25** (3), 034101.
- HARBIG, R.R., SHERIDAN, J. & THOMPSON, M.C. 2013 Reynolds number and aspect ratio effects on the leading-edge vortex for rotating insect wing planforms. *J. Fluid Mech.* **717**, 166–192.
- JARDIN, T. 2017 Coriolis effect and the attachment of the leading edge vortex. *J. Fluid Mech.* **820**, 312–340.
- JARDIN, T. & COLONIUS, T. 2018 On the lift-optimal aspect ratio of a revolving wing at low Reynolds number. *J. R. Soc. Interface* **15** (143), 20170933.
- JARDIN, T. & DAVID, L. 2014 Spanwise gradients in flow speed help stabilize leading-edge vortices on revolving wings. *Phys. Rev. E* **90** (1), 013011.
- JARDIN, T. & DAVID, L. 2015 Coriolis effects enhance lift on revolving wings. *Phys. Rev. E* **91** (3), 031001.
- JEONG, J. & HUSSAIN, F. 1995 On the identification of a vortex. *J. Fluid Mech.* **285**, 69–94.
- KIM, D. & GHARIB, M. 2010 Experimental study of three-dimensional vortex structures in translating and rotating plates. *Exp. Fluids* **49** (1), 329–339.
- LENTINK, D. & DICKINSON, M.H. 2009 Rotational accelerations stabilize leading edge vortices on revolving fly wings. *J. Expl Biol.* **212** (16), 2705–2719.
- MOU, X., LIU, Y. & SUN, M. 2011 Wing motion measurement and aerodynamics of hovering true hoverflies. *J. Expl Biol.* **214** (17), 2832–2844.
- OZEN, C.A. & ROCKWELL, D.O. 2012 Three-dimensional vortex structure on a rotating wing. *J. Fluid Mech.* **707**, 541–550.
- SANE, S.P. 2003 The aerodynamics of insect flight. *J. Expl Biol.* **206** (23), 4191–4208.
- SHYY, W. & LIU, H. 2007 Flapping wings and aerodynamic lift: the role of leading-edge vortices. *AIAA J.* **45** (12), 2817–2819.
- SUN, M. 2014 Insect flight dynamics: stability and control. *Rev. Mod. Phys.* **86** (2), 615–646.

Re effects on LEV formation and stability in revolving wings

- SUN, M. & WU, J. 2004 Large aerodynamic forces on a sweeping wing at low Reynolds number. *Acta Mechanica Sin.* **20** (1), 24–31.
- WEIS-FOGH, T. 1973 Quick estimates of flight fitness in hovering animals, including novel mechanisms for lift production. *J. Expl Biol.* **59** (1), 169–230.
- WERNER, N.H., CHUNG, H., WANG, J., LIU, G., CIMBALA, J.M., DONG, H. & CHENG, B. 2019 Radial planetary vorticity tilting in the leading-edge vortex of revolving wings. *Phys. Fluids* **31** (4), 041902.
- WERNER, N.H., WANG, J., DONG, H., PANAH, A.E. & CHENG, B. 2020 Scaling the vorticity dynamics in the leading-edge vortices of revolving wings with two directional length scales. *Phys. Fluids* **32** (12), 121903.
- WOJCIK, C.J. & BUCHHOLZ, J.H.J. 2014 Vorticity transport in the leading-edge vortex on a rotating blade. *J. Fluid Mech.* **743**, 249–261.
- WOLFINGER, M. & ROCKWELL, D.O. 2014 Flow structure on a rotating wing: effect of radius of gyration. *J. Fluid Mech.* **755**, 83–110.
- WU, J., CHEN, L., ZHOU, C., HSU, S.-J. & CHENG, B. 2019 Aerodynamics of a flapping-perturbed revolving wing. *AIAA J.* **57** (9), 3728–3743.
- WU, J. & SUN, M. 2004 Unsteady aerodynamic forces of a flapping wing. *J. Expl Biol.* **207** (7), 1137–1150.